Multidecadal Change of the South Pacific Gyre Circulation

DEAN ROEMMICH AND JOHN GILSON

Scripps Institution of Oceanography, University of California San Diego, La Jolla, California

PHILIP SUTTON

National Institute of Water and Atmospheric Research, Wellington, New Zealand

NATHALIE ZILBERMAN

Scripps Institution of Oceanography, University of California San Diego, La Jolla, California

(Manuscript received 3 December 2015, in final form 21 March 2016)

ABSTRACT

Multidecadal trends in ocean heat and freshwater content are well documented, but much less evidence exists of long-term changes in ocean circulation. Previously, a 12-yr increase, 1993 to 2004, in the circulation of the South Pacific Subtropical Gyre interior was described. That analysis was based on differences between early Argo and 1990s hydrographic data and changes in sea surface height. Here, it is shown that the trend of increasing circulation continues through 2014, with some differences within the Argo decade (2005 to 2014). Patterns that indicate or are consistent with increasing equatorward transport in the eastern portion of the South Pacific Gyre are seen in Argo temperature and steric height, Argo trajectory velocity, altimetric sea surface height, sea surface temperature, sea level pressure, and wind stress. Between 2005 and 2014 the geostrophic circulation across 35°S, from 160°W to South America, was enhanced by 5 Sv (1 Sv $\equiv 10^6$ m^3 s^{-1}) of added northward flow. This was countered by a southward transport anomaly between the date line and 160°W. Corresponding temperature trends span the full 2000-m depth range of Argo observations. The 22-yr trend, 1993 to 2014, in sea surface height at 35°S, 160°W is 8 cm decade^{-1}. Trends in sea surface temperature over 34 yr, 1981 to 2014, show a similar spatial pattern to that of sea surface height, with an increase of 0.5°C decade^{-1} at 35°S, 160°W. These multidecadal trends support the interpretation of the 40°S maximum in global ocean heat gain as resulting from anomalous wind forcing and Ekman convergence.

1. Introduction

The subtropical gyres are the dominant large-scale features of the midlatitude oceans. Their anticyclonic circulations, consisting of narrow, poleward western boundary currents (WBCs) and basinwide equatorward interior flows, play roles in maintaining Earth's climate and ecosystems. The WBCs carry warm water of tropical origin to higher latitudes where large quantities of heat are released to the atmosphere (e.g., Yu and Weller 2007). The cooler equatorward interior flows are the primary return path of the circulation in the oceanic mass budget. These contrasting warm and cool meridional circulations combine in exporting heat from the tropics to the midlatitudes (Zilberman et al. 2014). Most of the world's population lives in the latitude range of the subtropical gyres, and the ocean's heat transport, together with the moderating influence of the sea through its enormous heat capacity, contribute to setting the terrestrial climate of the subtropical latitudes. The subtropical gyre interiors, with their wind-driven convergent surface layers, are among the least biologically productive regions of the ocean, while the more energetic western and eastern boundary regions are biologically rich (Longhurst et al. 1995). These physical and biological attributes make the subtropical gyre circulations critical components of the biosphere and the climate system.

Denotes Open Access content.

Corresponding author address: Dean Roemmich, Scripps Institution of Oceanography, University of California San Diego, 9500 Gilman Drive, La Jolla CA 92093-0230.
E-mail: droemmich@ucsd.edu

DOI: 10.1175/JPO-D-15-0237.1

Although there is conclusive evidence of multidecadal changes in regional and global ocean temperature and salinity, there is much less to support changes in ocean circulation (Rhein et al. 2013). The net heat gain by the ocean of about 0.7 W m^{-2} (Wijffels et al. 2016), averaged over Earth's surface area, accounts for over 90% of Earth's excess of incoming over outgoing radiation (Rhein et al. 2013). Changes in the global pattern of surface salinity are consistent with intensification of the global pattern of evaporation minus precipitation (Hosoda et al. 2009; Durack et al. 2012) and hence of the atmospheric transport of water vapor. In the case of ocean circulation, a difficulty for observing long-term variability and trends is the nature of the required observations. That is, datasets consisting of velocity observations, or indirect estimates of geostrophic velocity based on gradients in geopotential height, are noisier than estimates of the spatial property means—they have "whiter" wavenumber spectra. That means a multidecadal trend in temperature is easier to detect with confidence than a trend in the horizontal gradient of temperature. In a few locations where long time series of transport have been obtained, such as the 50-yr record of Florida Current transport, no trend is seen (Rhein et al. 2013). The Intergovernmental Panel on Climate Change Fifth Assessment Report stated (Rhein et al. 2013, their section 3.6.6, p. 285), "Given the short duration of direct measurements of ocean circulation, we have very low confidence that multidecadal trends can be separated from decadal variability." Thus, an important goal for sustained ocean observations is to obtain datasets that are appropriate for resolving changes in ocean circulation as well as the changes in temperature, salinity, and density.

A prominent feature of the spatial pattern of global ocean heat gain since the 1990s World Ocean Circulation Experiment (WOCE) is that most of the global warming has occurred south of 20°S (Sutton and Roemmich 2011; Chen and Tung 2014) with a maximum in zonally averaged heat gain at 40°S in Argo data (Roemmich et al. 2015). This maximum is because of the warming at midlatitudes in all three Southern Hemisphere oceans, with the midlatitude South Pacific anomaly being especially strong. The present work is a "downscaling" from the global perspective to a regional one, as this will help to understand the advective mechanism of heat redistribution in the ocean that plays a prominent role in the spatial pattern of global ocean heat gain (Cai et al. 2010).

In previous work, Roemmich et al. (2007) compared steric height and trajectory data from early Argo profiles (2003 to 2005) with that from the WOCE (1991 to 1996) hydrographic survey. An increase in the subtropical gyre circulation was described based on a positive steric height anomaly centered at 40°S, 170°W. This analysis had observational limitations that included a temporal spread of 6 yr in the WOCE one-time survey together with a seasonal bias toward summertime, and the limited number of Argo profiles available at that time in the subtropical South Pacific domain. A total of 8751 Argo profiles were used, with an average of fewer than two profiles per 1° square for the 3-yr period. Altimetric sea surface height (SSH) provided the spatial and temporal context to link the WOCE and Argo datasets as well as confirmation of the steric height signal. SSH changes showed a similar pattern to steric height changes, with an increase over the 12-yr period from 1993 to 2004 of about 10 cm near the center of the feature.

The present study exploits the enormously expanded Argo dataset to demonstrate that the anticlockwise ocean circulation anomaly has continued to grow during the 2005 to 2014 Argo decade. With Argo near its designed coverage density, there are about four temperature–salinity profiles per 1° square added every year (Riser et al. 2016) plus a similar number of trajectory–velocity estimates. This higher data density diminishes the limitations of the earlier study with respect to spatial and temporal coverage. As in the earlier study, the SSH time series provides valuable context for steric height and extends the record to 22 yr. Even longer time series are available for sea surface temperature (SST), sea level pressure (SLP), and wind stress, and these provide evidence that the oceanic signal is wind driven and extends over more than 30 yr, although some changes in the spatial pattern are seen in the recent decade relative to the earlier study.

The oceans respond more readily to low-frequency wind forcing (interannual to decadal periods) than to higher-frequency wind forcing and thus act as a low-pass filter for atmospheric variability (e.g., Anderson and Corry 1985). As a result, multidecadal changes in atmospheric circulation may be more apparent in the oceanic responses than directly as changes in the noisier atmospheric forcing. In the South Pacific region, atmospheric observations are very sparse. There is limited evidence of a multidecadal southward shift and intensification of the midlatitude zonal westerly winds, although atmospheric reanalyses differ from one another on this issue (Swart and Fyfe 2012). Ultimately, confidence in and understanding of any possible long-term trend, together with implications for climate variability and change, will depend on consistent observations of both the atmospheric forcing and the oceanic response.

In the following section, the datasets used in the present analysis are described. Section 3 presents

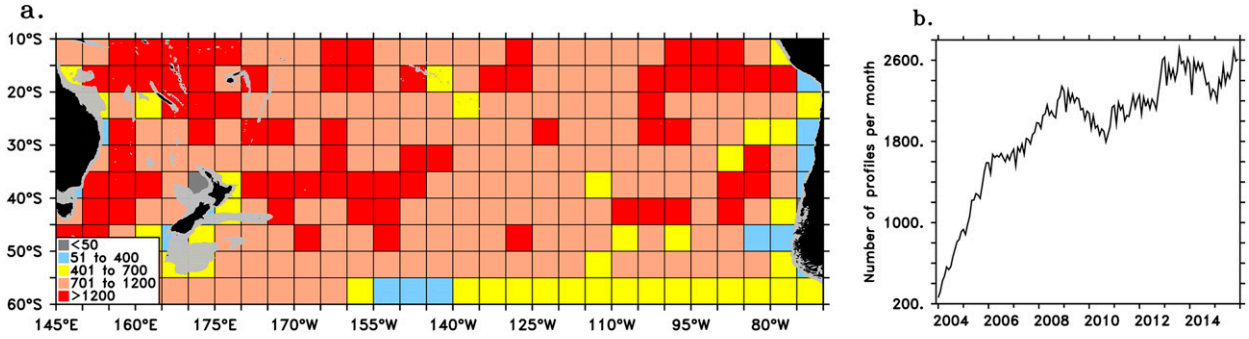

FIG. 1. (a) Total number of Argo profiles per 5° square in the South Pacific, 2004 to 2015. Light gray regions are shallower than 1000 m. (b) Argo profiles per month in the South Pacific domain 60° to 10°S, 145°E to 70°W.

results, beginning with the temporal extension of SSH and steric height records in relation to the Roemmich et al. (2007) analysis, and then considers accompanying changes in circulation, both for relative geostrophic velocity and 1000-dbar velocity derived from Argo trajectory data. Finally, patterns in sea surface temperature and sea level pressure trends over 34 yr are compared with those in the recent 10-yr Argo and 22-yr SSH records to suggest that the South Pacific anomaly has a multidecadal time scale. Discussion and conclusions are presented in the final section.

2. Data

a. *Argo profiles and trajectories*

Argo temperature–salinity (T–S) profile data and trajectory-based velocity data were used for the period from 2004 to 2015. The T–S data were subjected to quality control procedures as described in Roemmich and Gilson (2009), with best quality data being retained and interpolated onto a 1° × 1° monthly grid using optimal interpolation (Roemmich and Gilson 2009). Over 200 000 Argo profiles and trajectories from the domain 60° to 10°S and 145°E to 70°W, distributed fairly uniformly, were used in this study (Fig. 1).

Recent improvements have been made in the quality and completeness of Argo trajectory data (Ollitrault and Colin de Verdière 2014), and most Argo Data Assembly Centers are now creating data files containing the position and timing data needed for accurate velocity estimation. We included trajectory data from the southwest Pacific for the period 2004 to 2015, removing cycles that lacked necessary position or timing data. For the region 40° to 20°S and 140°E to 70°W, a total of 1113 floats were examined, and 801 of these yielded 83 747 individual trajectories used in the velocity estimation. Primary reasons for rejection were (i) insufficient surface positions for extrapolation, (ii) drift pressure not in the range 900 to 1200 dbar, (iii) no position accuracy information, and (iv) float on the APEX notification list for bad ascent end time or clock drift. For Argos-communicating floats that were retained, the surface trajectory was estimated using the method of Park et al. (2005). For Iridium floats, which have short surface times, first and last GPS fixes were used for the surface displacement.

b. *Sea surface height*

Gridded SSH anomaly products are provided by Archiving, Validation, and Interpretation of Satellite Oceanographic Data (AVISO). The delayed time product from two satellites was used, in which data have been merged for consistency at crossing points (Ducet et al. 2000). SSH data are continuous over the period January 1993 to December 2014. The SSH product was smoothed and regridded to the same to 1° × 1° monthly resolution as the gridded Argo profile data.

c. *Sea surface temperature, wind stress, and sea level pressure*

NOAA Optimum Interpolation Sea Surface Temperature version 2 (OISSTv2; Reynolds et al. 2002) for the period December 1981 to June 2015 was obtained from the NOAA Earth System Research Laboratory, Physical Sciences Division, on 21 July 2015.

Surface zonal wind stress and SLP are from the ERA-Interim product (Dee et al. 2011). Wind stress and SLP for the period coinciding with the SST product, 1981 to 2015, were extracted on 11 March 2015.

3. Results

a. *The anomalies in sea surface height, steric height, and temperature*

In the earlier work (Roemmich et al. 2007) the South Pacific SSH differences, consisting of 2-yr averages

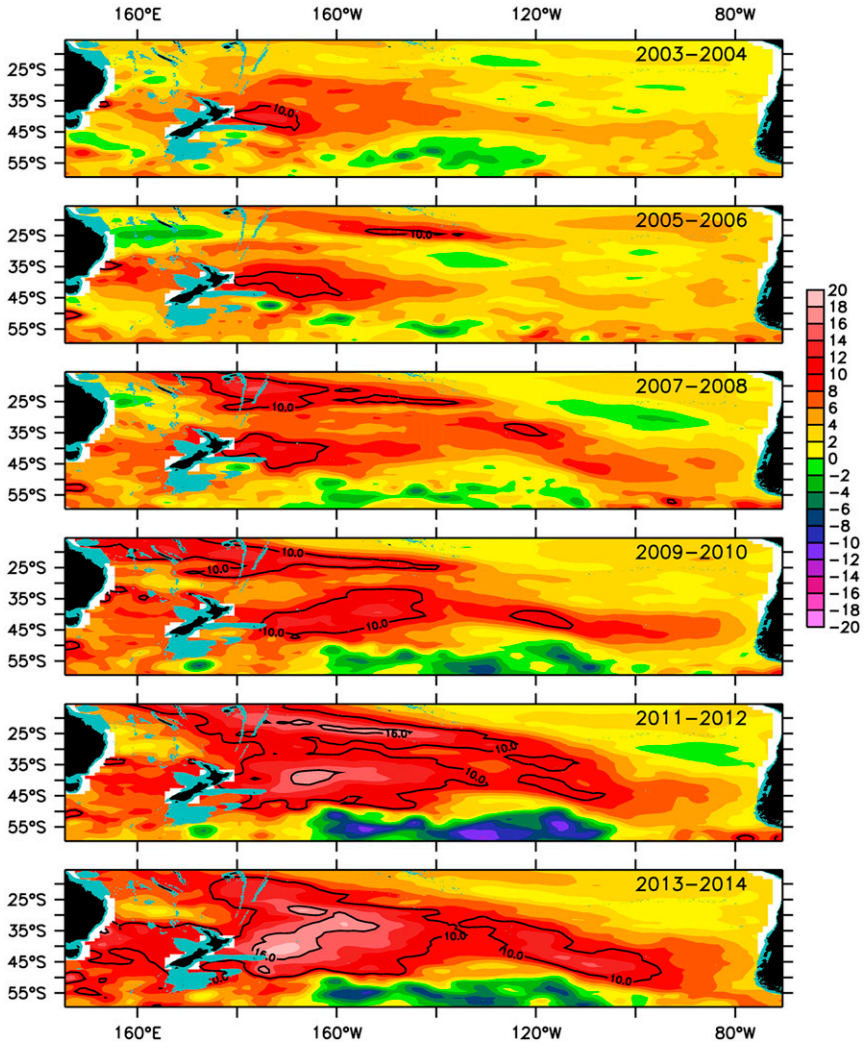

FIG. 2. Sea surface height anomaly (cm) for 2-yr averaging periods, as labeled in the upper-right corner of each panel; all are relative to the base period 1993 to 1994. Contour lines are drawn for 10 and 16 cm.

relative to a base period of 1993 to 1994, were examined (their Fig. 1). A spatially nonuniform increase in SSH was seen in the differences, culminating in a maximum of 10 cm around 40°S, 170°W, decreasing eastward to about 2 cm along the South American coast for the 10-yr difference. The same 10-yr SSH change, 2003 to 2004 minus 1993 to1994, is reproduced here in Fig. 2, along with the subsequent 2-yr intervals relative to the same 1993 to 1994 base period. During the second decade of observations the maximum difference in SSH has grown a further 10 cm to about 18 cm, with the strongest increases now centered around 35°S, 160°W. Thus, the pattern of SSH increase has continued through both decades of the 22-yr dataset, although its maximum has shifted eastward. Given that the difference in the mean steric height of the sea surface (0–2000 dbar) between the center of the South Pacific Gyre and the coast of South America is about 70 cm (Reid 1986; Roemmich and Gilson 2009), the 18-cm temporal SSH increase is a large anomaly, about 25% of the gyre interior topography. The pattern of SSH increase is robust. Similar spatial patterns are obtained (not shown) using a variety of analytical methods, including (i) differences calculated relative to the 22-yr mean rather than the initial 2-yr mean, (ii) the first empirical orthogonal function (EOF) of SSH, or (iii) the linear trend over 22 yr of SSH.

For the past decade, with good Argo coverage, between 2005 and 2014, SSH and steric height (0–2000 dbar) show similar spatial patterns in their linear temporal trends (Figs. 3a,b). The trends in SSH and steric height

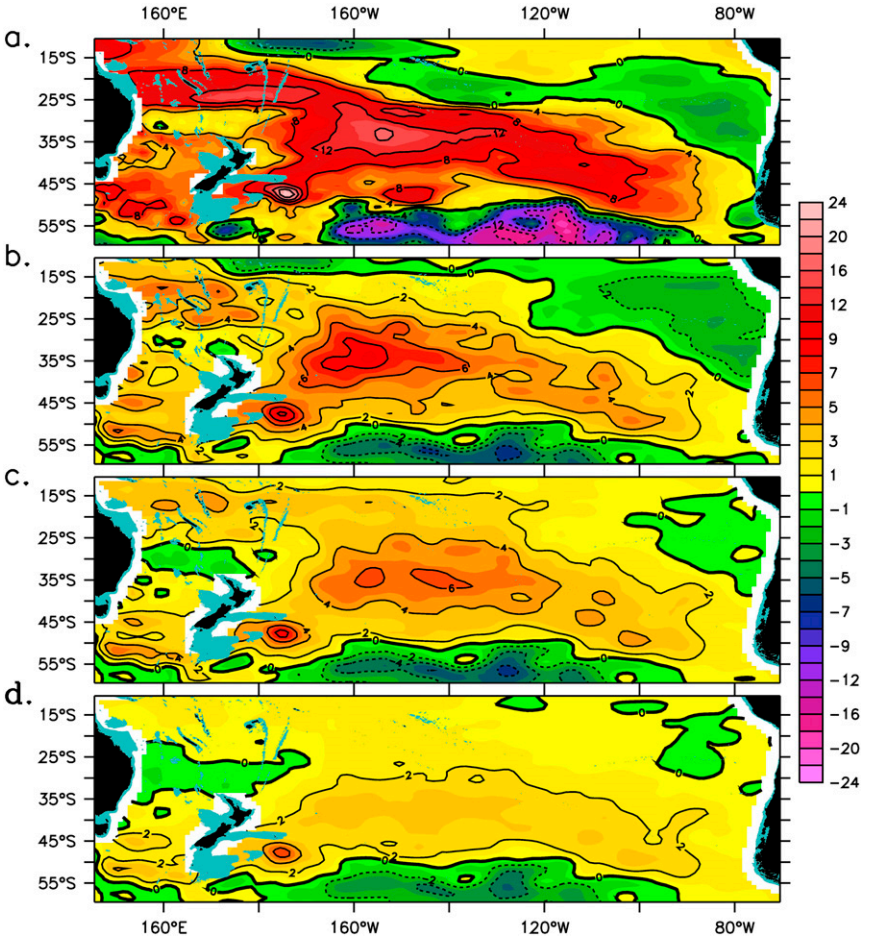

FIG. 3. Trends (cm decade^{-1}) during the period 2005 to 2014 in (a) SSH and in steric height (b) 0–2000, (c) 200–2000 , and (d) 500–2000 dbar. Contour lines are drawn at 4-cm intervals for SSH and 2-cm intervals for steric height.

both have zonally elongated structure extending from a maximum northeast of New Zealand with diminishing amplitude along an axis aligned toward the east-southeast. The trend is greater in SSH than in steric height, but even some details of the spatial patterns are similar in these independent datasets, such as the eddylike feature on the south side of Chatham Rise[1] near its eastern end. The increases in South Pacific SSH and steric height span most of the width of the midlatitude South Pacific Ocean. The density changes responsible for the steric height increase also extend over the full 0- to 2000-dbar range of Argo profiling, though diminishing in amplitude with increasing depth, so that the 500–2000-dbar steric height increase is much smaller than for 0–2000 dbar (Figs. 3b,d).

Near the maximum of the anomaly, at 35°S, 160°W, time series of the 12-month running mean of SSH and steric height are similar (Fig. 4) in their year-to-year variability as well as on the longer time scale but with larger magnitude in the SSH changes as noted above. The changes in SSH and steric height at this location were relatively small from 2005 to 2009 followed by large increases in 2010 and again in 2013. Since 2005, the overall increase in steric height is about 7 cm and about 10 cm in SSH. This proportionality in steric height to SSH variability is consistent with results from Sutton and Roemmich (2011) in the same latitude range. The SSH changes include the upper-ocean steric change observed by Argo plus deep steric change, below 2000 dbar, and changes in ocean mass.

The observed increases in steric height are predominantly (~90%) due to increases in temperature rather than to decreases in salinity. The linear trend in steric height at 35°S, 160°W for 2005 to 2015 is 8.0 cm decade^{-1}.

[1] Chatham Rise is the ridge extending east of New Zealand at about 45°S.

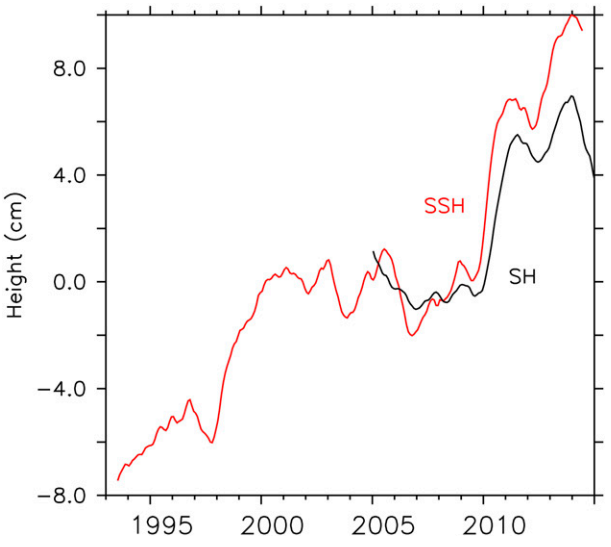

FIG. 4. Time series (cm, 12-month running mean) of SSH (red) and steric height (black, 0–2000 dbar) anomaly at 35°S, 160°W. The steric height series is adjusted to nearly coincide with SSH in 2005 to 2006.

This trend is not significantly different if the time-mean salinity is substituted for the time-varying salinity. The heat gain (Fig. 5a) reaches a maximum of $6 \pm 1\,\mathrm{W\,m^{-2}}$ at 35°S (0–2000 dbar), averaged from 170° to 130°W, decreasing to zero at 50° and 15°S. This strong heating rate along 35°S is an order of magnitude greater than the rate of global ocean heat gain during the Argo era ($0.7\,\mathrm{W\,m^{-2}}$; Wijffels et al. 2016). Indeed, the global zonally averaged heat gain also is a maximum at this latitude, about $2.7\,\mathrm{W\,m^{-2}}$ at 35°S (Roemmich et al. 2015). The linear trend (2005 to 2014) in subsurface temperature, averaged through the region of peak anomaly between 170° and 130°W, has a maximum value of $1°\mathrm{C\,decade^{-1}}$ at 35°S (Fig. 5b). This maximum is found at about 200-m depth on the $\sigma_\theta = 26.5$ potential density surface.

The occurrence of a maximum in heat gain along 35°S, either globally or regionally in the central Pacific, cannot be attributed to anomalous air–sea exchange (Cai et al. 2010) and must be caused mainly by vertical and/or horizontal displacement of the mean temperature field, most likely due to anomalous wind forcing. At 35°S, 160°W, the *T*–*S* relation at thermocline densities shifted toward higher temperature or lower salinity between initial (2005 to 2006) and final (2013 to 2014) 2-yr periods (Fig. 5c). This *T*–*S* shift, if resulting from anomalous property changes when the water parcels were on the sea surface, would require a ''pure warming'' (Bindoff and McDougall 1994) of 0.25°C or conversely a ''pure freshening'' of 0.025 in salinity. The $1°\mathrm{C\,decade^{-1}}$

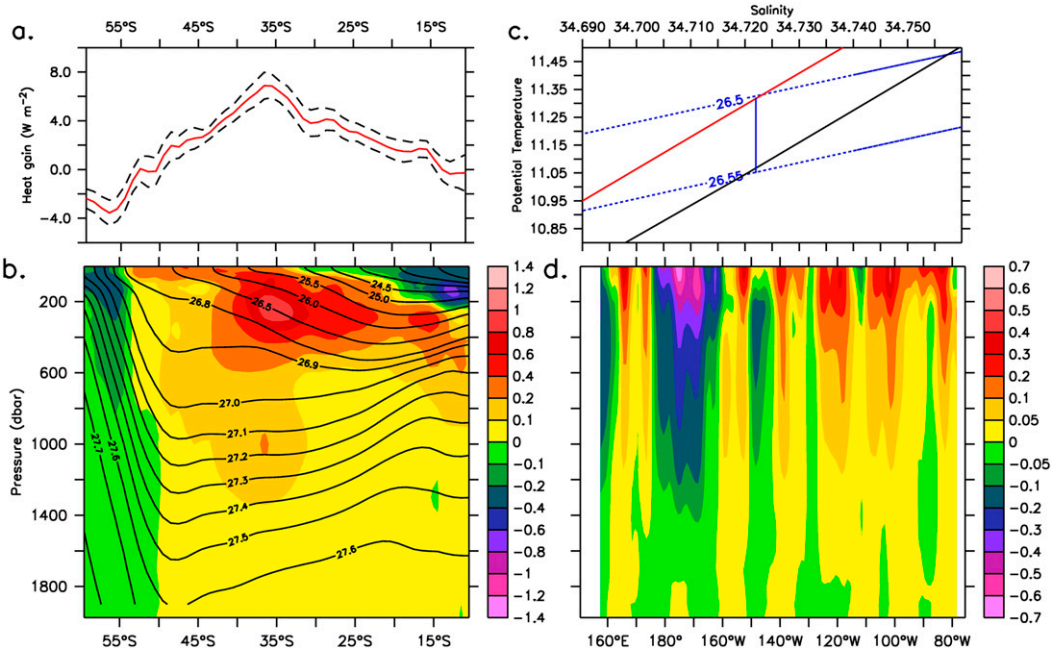

FIG. 5. (a) Heat gain ($\mathrm{W\,m^{-2}}$) from the linear trend in heat content, averaged between 170° and 130°W, for the period 2005 to 2014, with ±1 standard error (dashed line). (b) Linear trend in temperature for the period 2005 to 2014, averaged between 170° and 130°W (colors, $°\mathrm{C\,decade^{-1}}$). Contour lines are the 2005 to 2014 mean potential density. (c) *T*–*S* relation for part of the thermocline, averaged from 170° to 130°W, for 2005 to 2006 (black line) and for 2013 to 2014 (red line). Dashed blue lines indicate potential density surfaces as labelled. (d) Linear trend in meridional geostrophic velocity ($\mathrm{cm\,s^{-1}\,decade^{-1}}$) at 35°S, smoothed by a 10° longitude running mean, relative to 2000 dbar.

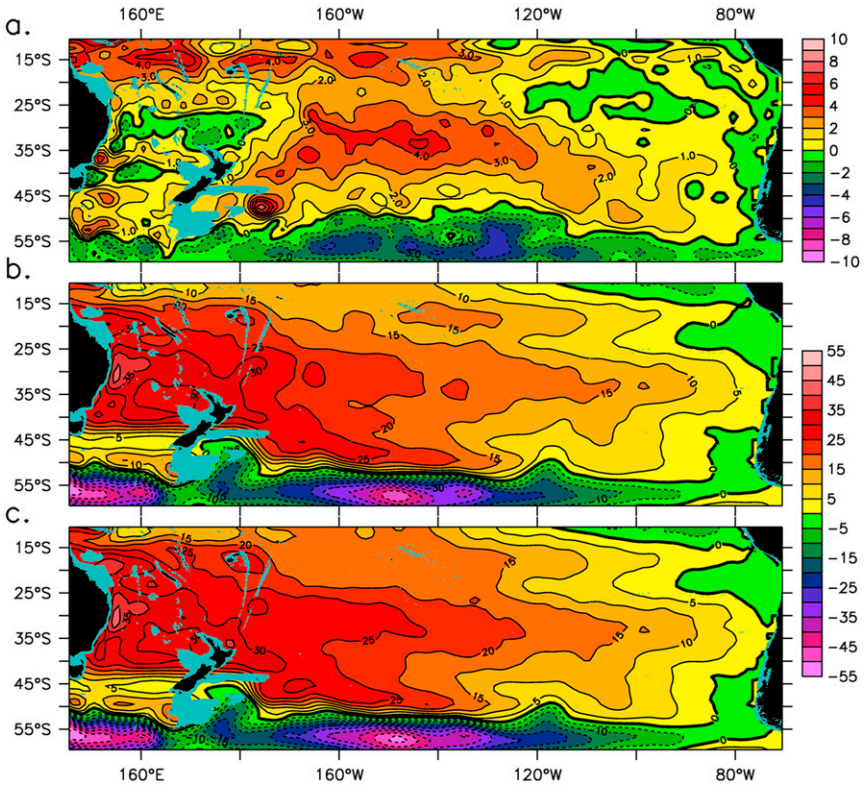

FIG. 6. Meridional geostrophic transport (Sv, 0–2000 dbar relative to 2000 dbar) integrated from the coast of South America westward. (a) Difference between the 2-yr periods 2013 to 2014 and 2005 to 2006. (b) Mean for 2005 to 2006. (c) Mean for 2013 to 2014.

maximum warming in the thermocline (Fig. 5b) is much larger. Deeper in the water column, the fraction of *T*–*S* change that could be attributable to pure warming decreases further, and the large heat gain implicates displacement of the mean temperature field as the dominant mechanism.

Southward displacement of the mean temperature field could account for the thermocline warming signal since the thermocline shoals toward the south at 35°S (averaged from 170° to 130°W; Fig. 5b). However, looking deeper into the water column, the intermediate depth maximum warming rate occurs where the isotherms and isopycnals (e.g., σ_θ = 27.1 potential density) are slightly sloping in the opposite sense. Thus, a simple southward shift of the mean temperature field cannot account for the observed signals. The observed shifts in *T*–*S* demonstrate that downward displacement cannot be the only process involved in the observed warm anomalies, but wind-driven convergence causing downward displacement of isotherms/isopycnals is probably the largest contributor (section 4). Local trends in the depth of isopycnals range up to 80 m decade^{-1} at 40°S on the σ_θ = 26.9 potential density surface.

b. *The anomaly in ocean circulation*

The presence of maxima in SSH and steric height increases at about 35°S, 160°W (Fig. 3) indicates a geostrophic circulation and transport anomaly consisting of an anticlockwise rotation around that central location. That is, on the sea surface an equatorward velocity anomaly across 35°S between 160°W and South America is offset by a poleward velocity anomaly between 160°W and northern New Zealand (175°E), where the SSH anomaly decreases to zero. The 2005 to 2014 trend in meridional geostrophic velocity relative to 2000 dbar (Fig. 5d) shows this pattern with surface-intensified trends up to about $\pm 0.6\,\mathrm{cm\,s^{-1}}$ decade^{-1} in each of the broad regions east and west of 160°W. West of 175°E in the Tasman Sea, the velocity trend is mostly positive.

The change in geostrophic transport, 2013 to 2014 minus 2005 to 2006 and relative to 2000 dbar, is estimated by converting steric height to meridional geostrophic velocity, integrating the velocity in depth, and then integrating the transport westward from the South American coast in each time period and for the difference (Fig. 6). The equatorward transport difference

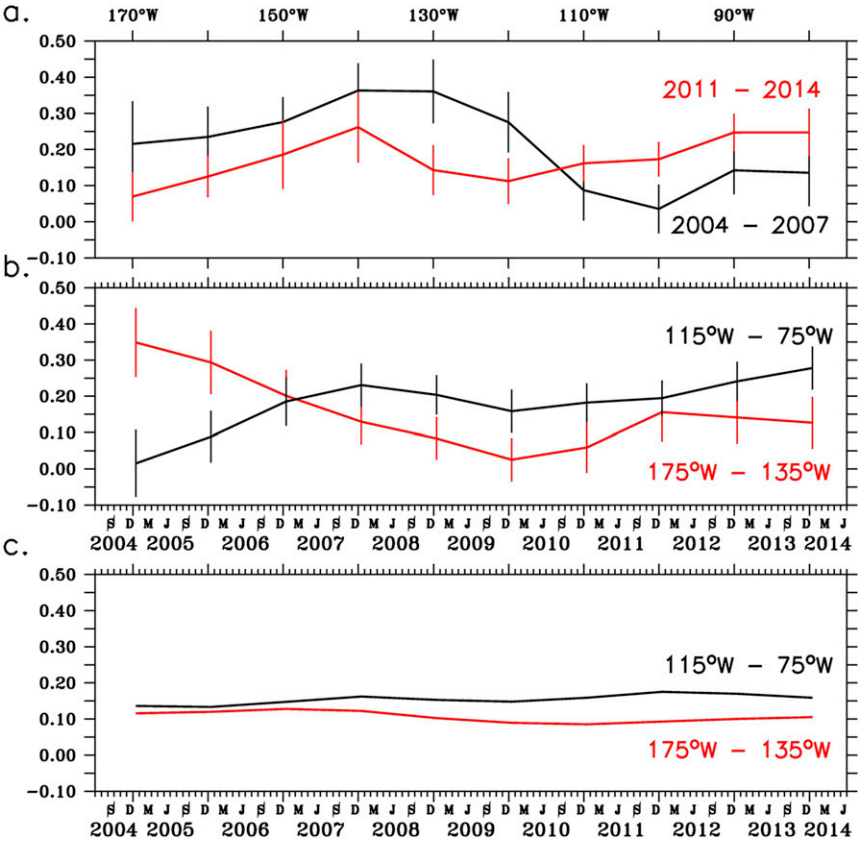

FIG. 7. Meridional velocity (cm s^{-1}) at 1000 dbar. (a) Longitude-dependent binned average of meridional trajectory velocity, 40° to 30°S, in overlapping 20° longitude bins for 2004 to 2007 (black) and 2011 to 2014 (red). Error bars are ±1 standard error. (b) Time series of meridional trajectory velocity, 40° to 30°S, in overlapping 2-yr time bins for 115° to 75°W (black) and 175°W to 135°W (red). (c) Space–time averaging as in (b), but for geostrophic velocity at 1000 dbar relative to 2000 dbar based on Argo profile data.

accumulates to 5 Sv (1 Sv = 10^6 m^3 s^{-1}) between South America and 145°W and then decreases to zero north of New Zealand. Maps of the transport integral for the two time periods (Figs. 6b,c) are noticeably different from one another, underlining that the 5-Sv difference between them is a significant fraction of the interior gyre transport. Moreover, the transport anomaly pattern is primarily superimposed on the northern half of the ''C-shaped'' subtropical gyre. The fact that the maximum in the zonally integrated transport difference (Fig. 6a) is farther east than the maximum in ΔSSH (Fig. 3a) indicates that the center of the geostrophic velocity anomaly tends eastward with increasing depth.

In addition to the relative geostrophic velocity and transport, consistent circulation changes are also observed in the absolute meridional velocity at 1000 dbar based on Argo trajectory data. The velocity data are noisy, and it was necessary to average over broad longitude, latitude, and time bins to reduce noise. First, it was noted that the trajectory data, averaged from 40° to 30°S, show an increase in northward velocity for 20° longitude bins centered east of 115°W and a decrease for bins centered west of 115°W (Fig. 7a). Here, the black line shows these bin averages for the 4-yr interval 2004 to 2007 and the red line for 2011 to 2014. Then, time series of bin-averaged meridional velocity were constructed (Fig. 7b) for the 40° longitude ranges 175° to 135°W (red line) and 115° to 75°W (black line), averaged yearly over 2-yr time bins. The binned 10-day trajectory estimates were assumed to contain $N/2$ degrees of freedom (Ollitrault and Colin de Verdière 2014), and the vertical bars in Fig. 7 represent one standard error. The northward velocity increase in the eastern longitudes and the decrease in the western band are at best marginally significant in individual bins. However, the similarity over multiple adjoining bins and the consistency of these estimates with the steric height findings of an anticlockwise increase in the interior ocean circulation makes this

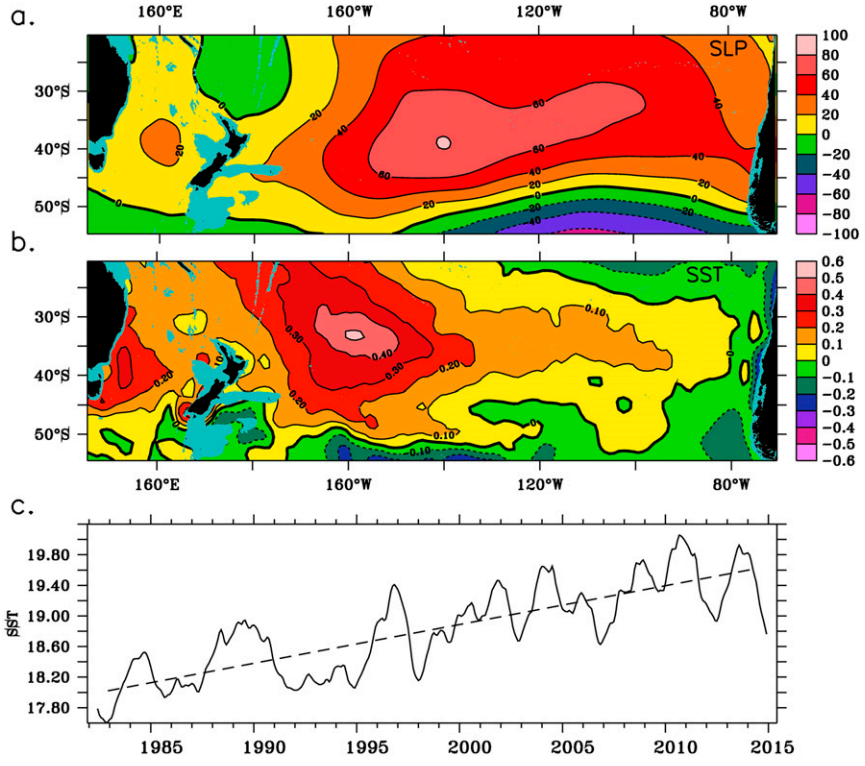

FIG. 8. Linear trend for 1981 through 2015, in (a) SLP (Pa decade^{-1}, ERA-Interim reanalysis), (b) SST (°C decade^{-1}, NOAA OISSTv2 product). (c) Time series of SST (°C, 12-month running mean) at the location of maximum trend (33°S, 158°W).

result more compelling. As noted above in the steric height discussion, the center of the anomalous circulation is farther east at 1000 dbar than at the sea surface.

For a further comparison of steric height and velocity data, the meridional geostrophic velocity at 1000 dbar relative to 2000 dbar was averaged over the same 10° latitude by 40° longitude and 2-yr time bins as the trajectory data (Fig. 7c). Although a small increase in the northward velocity in the east (black line) and a small decrease in the west (red line) are seen, the magnitude of changes is less than in the trajectory velocity. This is at least partially attributable to the 2000-dbar reference level. The South Pacific Gyre extends to about 3500 m (Reid 1986), and we have seen that the temperature trend observed in the Argo era also extends to 2000 m (Fig. 5b) and likely deeper. On these bases, it is unsurprising that the geostrophic velocity at 1000 dbar relative to 2000 dbar and its decadal change are underestimates of the absolute 1000-dbar velocity and its change.

c. *Multidecadal sea level pressure and sea surface temperature*

The 22-yr spatial pattern of SSH increase was described in Fig. 2, along with a similar spatial pattern of 10-yr changes in subsurface temperature, steric height, and 1000-dbar absolute velocity observed by Argo (Figs. 3–7). An important question is whether these changes are the result of decadal variability or whether they are part of a multidecadal trend. For context on a longer time-scale, linear trends in SLP (Fig. 8a) and SST (Figs. 8b,c) are examined for the period starting in late 1981. This was the beginning of the satellite era in SST observation and of the NOAA Optimum Interpolation SST version 2 product that combines satellite and in situ observations (Reynolds et al. 2002). The spatial pattern of the SST trend over the 34-yr period 1981 to 2014 (Fig. 8b) is remarkably similar to that seen in the shorter SSH and steric height records, with a maximum of 0.5°C decade^{-1} at 33°S, 158°W, near the same location as the maxima of the SSH and steric height fields. A time series of SST at that location (Fig. 8c) shows that the 34-yr increase is greater in magnitude than the interannual and decadal variability within the record. An increase in SST is consistent with the observed downward displacement of the thermocline. The trend in SLP also shows a broad maximum in the central South Pacific. The maximum, about 100 Pa decade^{-1}, is offset to the southeast of those in SST, SSH, and steric height

but is consistent in pattern with an anomalous anticyclonic anomaly in the surface wind field. The corresponding anomalies in surface wind stress are also consistent with forcing the ocean circulation anomalies described earlier.

4. Discussion

Similar spatial patterns were observed in the 10-yr increase in South Pacific steric height (Fig. 3), the corresponding 22-yr increase in SSH (Fig. 2), and the 34-yr increase in SST (Fig. 8). The anomaly patterns were zonally elongated at 35°S, occupying most of the basin, with maxima located near 160°W of about 8 cm over 10 yr in steric height, 18 cm over 22 yr in SSH, and 1.7°C over 34 yr in SST. These variables are dynamically related to one another, but the respective observing systems are independent as well as being of differing durations. The similarity in spatial patterns and the continuity over time in the 22- and 34-yr time series are indicators that the 10-yr trends in subsurface temperature, steric height, and velocity observed by Argo are multidecadal.

Sasaki et al. (2008) suggested that the South Pacific SSH increase in the period 1993 to 2003 was due to decadal variability rather than a long-term trend. This was based on strong similarity between the time series of a model-derived EOF and that of SSH projected onto the same EOF. An extended time series of the model EOF beginning in 1970 showed no trend over the long record, and the 1993 to 2003 increase therefore appeared to be a decadal fluctuation (Sasaki et al. 2008, their Fig. 3). Here, the contrary evidence is in the 34-yr SST trend and also with the SSH time series now being two decades long. The second decade of SSH reinforces, rather than reverses, the signal, and the full 22-yr SSH dataset shows a similar spatial pattern of increase. There is undoubtedly decadal as well as interannual variability in the large-scale patterns, but the observational evidence argues for an element of multidecadal change.

Subsurface variability includes downward displacement of isothermal and isopycnal surfaces, at rates up to 80 m decade^{-1}, extending with decreasing amplitude through the water column to at least 2000 dbar. Maxima in subsurface temperature change were 1°C decade^{-1} in the thermocline (σ_θ = 26.5) and 0.2°C decade^{-1} in the Antarctic Intermediate Water layer (σ_θ = 27.1). In addition to trends in temperature, a similar mid-Pacific trend of increasing sea surface salinity was observed in Argo data, with a maximum of 0.25 decade^{-1} at 35°S, 125°W, consistent with the 50-yr trend described by Durack and Wijffels (2010).

The observed anomaly patterns in SSH and steric height are largely caused by wind-driven convergence of the surface layer and resultant downward displacement (Ekman pumping) of the thermocline and deeper layers. In Fig. 9a, the time-varying SSH anomaly at 35°S for 1993 to 2014 is shown relative to a base averaging period of 1993 to 2004. The Ekman pumping velocity (Fig. 9b; m yr^{-1} downward) is calculated from wind stress (ERA-Interim) as the wind stress curl divided by the product of density times the Coriolis parameter. The temporal evolution of SSH along 35°S (Fig. 9a) consists of localized wind-forced features (Fig. 9b) but with clear indications in SSH of westward propagation (Qiu and Chen 2006). It is seen, from comparing Figs. 9a and 9b, that the large increases in SSH at around 110°W in 2007 and 2010 through 2013 are the result of localized Ekman pumping, with the SSH anomalies subsequently propagating westward about 10° of longitude per year.

Averaged over the 2004 to 2014 period, relative to 1993 to 2004, the anomalous Ekman vertical velocity is upward between the date line and 140°W and downward between 120° and 80°W. This pattern of anomalous Ekman pumping—strengthening in the east and weakening in the central ocean—differs from the previous decade discussed in Roemmich et al. (2007, their Fig. 10), when the Ekman pumping increased across all of the gyre interior. The anomaly patterns of SSH and steric height described in section 3a are consistent with the anomalies in wind stress curl. To take this a step farther, Sverdrup transport is calculated from the wind stress curl. The geostrophic component of Sverdrup transport [e.g., Gray and Riser 2014, their Eq. (5)] is the difference between the Sverdrup (total) transport and ageostrophic Ekman transport:

$$\text{Wind-driven geostrophic transport} = \frac{\mathbf{k}\cdot\nabla\times\boldsymbol{\tau}}{\rho\beta} + \frac{\tau^x}{\rho f},$$

where τ is the wind stress and τ^x is its zonal component; ρ is density; f is the Coriolis parameter; and β is the meridional derivative of f. The anomaly in wind-driven geostrophic transport is estimated here as the difference between 2013 to 2014 and 1993 to 2004 values (Fig. 9c) and is integrated from the South American coast westward. This calculation is, of course, sensitive to the years chosen but is nonetheless illustrative. A 5-Sv northward anomaly east of 160°W is seen as well as the largely offsetting southward anomaly between the date line and 160°W. This is much like the pattern in steric height and geostrophic transport anomaly from Argo (Fig. 6a). We are not claiming that the basinwide circulation of the South Pacific Gyre is in equilibrium with the wind forcing. Clearly, it is not (Fig. 9a). But with large variability on time scales longer than a decade, and that being the time scale for signals to cross the basin at 35°S, the adjustment process toward Sverdrup balance is seen

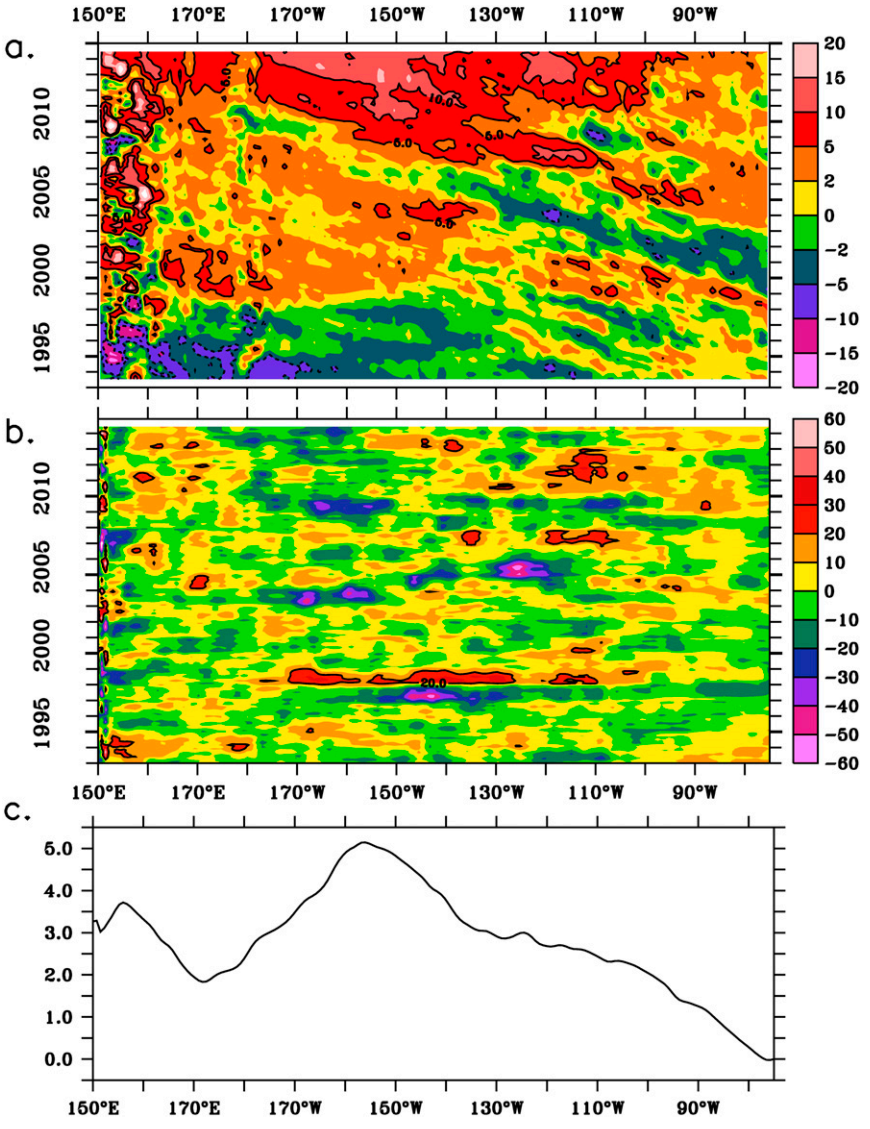

FIG. 9. (a) SSH anomaly (cm) along 35°S for 1993 to 2014 relative to the mean from 1993 to 2003. (b) Ekman pumping velocity anomaly at 35°S (m yr^{-1}, positive downward) for 1993 to 2014 relative to the mean from 1993 to 2003. (c) Meridional geostrophic Sverdrup transport anomaly (Sv), integrated westward from South America along 35°S, for 2013 to 2014 relative to the mean from 1993 to 2003.

taking place over periods comparable to those of the 10- and 22-yr datasets.

While the focus here is decadal to multidecadal variability, it is clear from the SSH and steric height time series at 35°S, 160°W (Fig. 4), and from the Ekman pumping time series (Fig. 9b), that interannual variability is also important. The sharp SSH increases in 1998–2000 and 2010 correspond with La Niña episodes, while decreases occurred most often in El Niño years. There is a visual similarity between a detrended SSH time series at 35°S, 160°W and the Niño-3.4 index (e.g., Trenberth 1997). However, the correlation is higher (r^2 = 0.22) between a zonally averaged (180°–90°W) SSH time series and Niño-3.4. The modest correlation increase in the zonal average reinforces the message from SSH and wind stress forcing (Fig. 9) that locally forced anomalies propagate westward.

In addition to the changes in circulation in the interior South Pacific, there is also strong interest in the boundary current region west of New Zealand. Decadal variability in the transport of the East Australian Current (EAC) at 34°S has been described over a 15-yr period of observations (Ridgway et al. 2008) and interpreted as variability in the distribution of EAC

transport between the southward EAC extension and the eastward separated flow along the Tasman Front (Hill et al. 2011). A 60-yr trend in temperature at the Maria Island coastal station east of Tasmania was found to be due to a wind-forced increase in the transport of the EAC extension (Hill et al. 2008). For the present study, the Argo dataset resolves the interior ocean transport and variability on interannual time scales, but not that of the EAC. Moreover, latitude 35°S passes through northern New Zealand, which interferes with the SSH propagation. In addition to local forcing and westward-propagating signals, there are complex interactions with topography in the west. In Fig. 5d, a positive trend is seen during the Argo era in smoothed meridional geostrophic velocity in the Tasman Sea. This trend reverses at the western boundary. There, a subsurface maximum in increasing southward flow is consistent with an increase in the EAC extension. Figure 9c shows a similar result in the decadal change in Sverdrup transport. That is, a northward change is seen over most of the Tasman Sea but with a reverse to southward in the western boundary region. These are decadal signals, and the relationship of SSH and steric height west of New Zealand with the pattern of long-term trends in the ocean interior is beyond the scope of the present study.

In Roemmich et al. (2007), we described the observed trends in SSH and steric height as a "spinup" of the South Pacific Gyre, and indeed there is an anticyclonic circulation anomaly of basin scale. However, more precisely, a spinup of the mean gyre circulation would require a net equatorward anomaly in the interior balanced by a poleward anomaly in the EAC. Although such an equilibrated, intensified gyre circulation may be the eventual result, the description here is of a transitional circulation, of a gyre undergoing adjustment to changing wind forcing and not one in equilibrium. Nevertheless, the multidecadal patterns in mid-South Pacific temperature, steric height, and sea surface height account for a substantial fraction of the accumulated heat in the global ocean and climate system (Roemmich et al. 2015; Cai et al. 2010; Wijffels et al. 2008).

Acknowledgments. The Argo data used here were collected and are made freely available by the International Argo Program and by the national programs that contribute to it. D. R., J. G., and N. Z., and their part in the Argo program, were supported by U.S. Argo through NOAA Grant NA10OAR4310139 (CIMEC/SIO Argo). We thank M. Scanderbeg for assistance with the Argo trajectory dataset. The statements, findings, conclusions, and recommendations herein are those of the authors and do not necessarily reflect the views of the National Oceanic and Atmospheric Administration or the Department of Commerce. The altimeter sea surface height products used here were produced by Ssalto/Duacs and distributed by AVISO with support from CNES. NOAA_OI_SST_V2 data were provided by the NOAA/OAR/ESRL PSD, Boulder, Colorado (from their website at http://www.esrl.noaa.gov/psd/). Wind stress and sea level pressure were from the ERA-Interim reanalysis products provided by the European Centre for Medium-Range Weather Forecasts (from their web site at http://apps.ecmwf.int/datasets/data/interim-full-moda/). Graphics were produced using Ferret, a product of NOAA's Pacific Marine Environmental Laboratory.

REFERENCES

Anderson, D., and R. Corry, 1985: Ocean response to low frequency wind forcing with application to the seasonal variation in the Florida Straits—Gulf Stream transport. *Prog. Oceanogr.*, **14**, 7–40, doi:10.1016/0079-6611(85)90003-5.

Bindoff, N., and T. McDougall, 1994: Diagnosing climate change and ocean ventilation using hydrographic data. *J. Phys. Oceanogr.*, **24**, 1137–1152, doi:10.1175/1520-0485(1994)024<1137:DCCAOV>2.0.CO;2.

Cai, W., T. Cowan, S. Godfrey, and S. Wijffels, 2010: Simulations of processes associated with the fast warming rate of the southern midlatitude ocean. *J. Climate*, **23**, 197–206, doi:10.1175/2009JCLI3081.1.

Chen, X., and K.-K. Tung, 2014: Varying planetary heat sink led to global-warming slowdown and acceleration. *Science*, **345**, 897–903, doi:10.1126/science.1254937.

Dee, D. P., and Coauthors, 2011: The ERA-Interim reanalysis: Configuration and performance of the data assimilation system. *Quart. J. Roy. Meteor. Soc.*, **137**, 553–597, doi:10.1002/qj.828.

Ducet, N., P.-Y. Le Traon, and G. Reverdin, 2000: Global high resolution mapping of ocean circulation from TOPEX/Poseidon and *ERS-1* and *-2*. *J. Geophys. Res.*, **105**, 19 477–19 498, doi:10.1029/2000JC900063.

Durack, P. J., and S. E. Wijffels, 2010: Fifty-year trends in global ocean salinities and their relationship to broad-scale warming. *J. Climate*, **23**, 4342–4362, doi:10.1175/2010JCLI3377.1.

——, ——, and R. J. Matear, 2012: Ocean salinities reveal strong global water cycle intensification during 1950 to 2000. *Science*, **336**, 455–458, doi:10.1126/science.1212222.

Gray, A. R., and S. C. Riser, 2014: A global analysis of Sverdrup balance using absolute geostrophic velocities from Argo. *J. Phys. Oceanogr.*, **44**, 1213–1229, doi:10.1175/JPO-D-12-0206.1.

Hill, K. L., S. R. Rintoul, R. Coleman, and K. R. Ridgway, 2008: Wind forced low frequency variability of the East Australia Current. *Geophys. Res. Lett.*, **35**, L08602, doi:10.1029/2007GL032912.

——, ——, K. R. Ridgway, and P. R. Oke, 2011: Decadal changes in the South Pacific western boundary current system revealed in observations and ocean state estimates. *J. Geophys. Res.*, **116**, C01009, doi:10.1029/2009JC005926.

Hosoda, S., T. Suga, N. Shikama, and K. Mizuno, 2009: Global surface layer salinity change detected by Argo and its implication for hydrological cycle intensification. *J. Oceanogr.*, **65**, 579–586, doi:10.1007/s10872-009-0049-1.

Longhurst, A., S. Sathyendranath, T. Platt, and C. Caverhill, 1995: An estimate of global primary production in the ocean from satellite radiometer data. *J. Plankton Res.*, **17**, 1245–1271, doi:10.1093/plankt/17.6.1245.

Ollitrault, M., and A. Colin de Verdière, 2014: The ocean general circulation near 1000-m depth. *J. Phys. Oceanogr.*, **44**, 384–409, doi:10.1175/JPO-D-13-030.1.

Park, J. J., K. Kim, B. A. King, and S. C. Riser, 2005: An advanced method to estimate deep currents from profiling floats. *J. Atmos. Oceanic Technol.*, **22**, 1294–1304, doi:10.1175/JTECH1748.1.

Qiu, B., and S. Chen, 2006: Decadal variability in the large-scale sea surface height field of the South Pacific Ocean: Observations and causes. *J. Phys. Oceanogr.*, **36**, 1751–1762, doi:10.1175/JPO2943.1.

Reid, J., 1986: On the total geostrophic circulation of the South Pacific Ocean: Flow patterns, tracers, and transports. *Prog. Oceanogr.*, **16**, 1–61, doi:10.1016/0079-6611(86)90036-4.

Reynolds, R. W., N. A. Rayner, T. M. Smith, D. C. Stokes, and W. Wang, 2002: An improved in situ and satellite SST analysis for climate. *J. Climate*, **15**, 1609–1625, doi:10.1175/1520-0442(2002)015<1609:AIISAS>2.0.CO;2.

Rhein, M., and Coauthors, 2013: Observations: Ocean. *Climate Change 2013: The Physical Science Basis*, T. F. Stocker et al., Eds., Cambridge University Press, 255–315.

Ridgway, K. R., R. C. Coleman, R. J. Bailey, and P. Sutton, 2008: Decadal variability of East Australian Current transport inferred from repeated high-density XBT transects, a CTD survey and satellite altimetry. *J. Geophys. Res.*, **113**, C08039, doi:10.1029/2007JC004664.

Riser, S., and Coauthors, 2016: Fifteen years of ocean observations with the global Argo array. *Nat. Climate Change*, **6**, 145–153, doi:10.1038/nclimate2872.

Roemmich, D., and J. Gilson, 2009: The 2004-2008 mean and annual cycle of temperature, salinity, and steric height in the global ocean from the Argo program. *Prog. Oceanogr.*, **82**, 81–100, doi:10.1016/j.pocean.2009.03.004.

——, ——, R. Davis, P. Sutton, S. Wijffels, and S. Riser, 2007: Decadal spinup of the South Pacific subtropical gyre. *J. Phys. Oceanogr.*, **37**, 162–173, doi:10.1175/JPO3004.1.

——, J. Church, J. Gilson, D. Monselesan, P. Sutton, and S. Wijffels, 2015: Unabated planetary warming and its ocean structure since 2006. *Nat. Climate Change*, **5**, 240–245, doi:10.1038/nclimate2513.

Sasaki, Y., S. Minobe, N. Schneider, T. Kagimoto, M. Nonaka, and H. Sasaki, 2008: Decadal sea level variability in the South Pacific in a global eddy-resolving ocean model hindcast. *J. Phys. Oceanogr.*, **38**, 1731–1747, doi:10.1175/2007JPO3915.1.

Sutton, P., and D. Roemmich, 2011: Decadal steric and sea surface height changes in the Southern Hemisphere. *Geophys. Res. Lett.*, **38**, L08604, doi:10.1029/2011GL046802.

Swart, N. C., and J. C. Fyfe, 2012: Observed and simulated changes in the Southern Hemisphere surface westerly wind-stress. *Geophys. Res. Lett.*, **39**, L16711, doi:10.1029/2012GL052810.

Trenberth, K., 1997: The definition of El Niño. *Bull. Amer. Meteor. Soc.*, **78**, 2771–2777, doi:10.1175/1520-0477(1997)078<2771:TDOENO>2.0.CO;2.

Wijffels, S., J. Willis, C. M. Domingues, P. Barker, N. J. White, A. Gronell, K. Ridgway, and J. A. Church, 2008: Changing expendable bathythermograph fall rates and their impact on estimates of thermosteric sea level rise. *J. Climate*, **21**, 5657–5672, doi:10.1175/2008JCLI2290.1.

——, D. Roemmich, D. Monselesan, J. Church, and J. Gilson, 2016: Ocean temperatures chronicle the ongoing warming of Earth. *Nat. Climate Change*, **6**, 116–118, doi:10.1038/nclimate2924.

Yu, L., and R. Weller, 2007: Objectively analyzed air–sea heat fluxes for the global ice-free oceans (1981–2005). *Bull. Amer. Meteor. Soc.*, **88**, 527–539, doi:10.1175/BAMS-88-4-527.

Zilberman, N. V., D. H. Roemmich, and S. T. Gille, 2014: Meridional volume transport in the South Pacific: Mean and SAM-related variability. *J. Geophys. Res. Oceans*, **119**, 2658–2678, doi:10.1002/2013JC009688.